Universal Synthetic Aperture Sequence for Anatomic, Functional and Super Resolution Imaging

Jørgen Arendt Jensen[1], *IEEE Fellow*, Borislav Gueorguiev Tomov[1], Lars Emil Haslund[1],
Nathalie Sarup Panduro[2] and Charlotte Mehlin Sørensen[2]

[1]Center for Fast Ultrasound Imaging, Department of Health Technology,
Technical University of Denmark, DK-2800 Lyngby, Denmark
[2]Department of Biomedical Sciences, University of Copenhagen, Denmark

Abstract—Synthetic Aperture (SA) can be used for both anatomic and functional imaging, where tissue motion and blood velocity are revealed. Often, sequences optimized for anatomic B-mode imaging are different from functional sequences, as the best distribution and number of emissions are different. B-mode sequences demand many emissions for a high contrast, whereas flow sequences demand short sequences for high correlations yielding accurate velocity estimates. This paper hypothesizes that a single, universal sequence can be developed for linear array SA imaging. This sequence yields high quality linear and non-linear B-mode images as well as accurate motion and flow estimates for high and low blood velocities and super resolution images. Interleaved sequences with positive and negative pulse emissions for the same spherical virtual source were used to enable flow estimation for high velocities and make continuous long acquisitions for low velocity estimation. An optimized pulse inversion (PI) sequence with 2×12 virtual sources was implemented for four different linear array probes connected to either a Verasonics Vantage 256 scanner or the SARUS experimental scanner. The virtual sources were evenly distributed over the whole aperture and permuted in emission order for making flow estimation possible using 4, 8, or 12 virtual sources. The frame rate was 208 Hz for fully independent images for a pulse repetition frequency of 5 kHz, and recursive imaging yielded 5,000 images per second. Data were acquired from a phantom mimicking the carotid artery with pulsating flow and the kidney of a Sprague-Dawley rat. Examples include anatomic high contrast B-mode, non-linear B-mode, tissue motion, power Doppler, color flow mapping, vector velocity imaging and super resolution imaging derived from the same data set and demonstrates that all imaging modes can be shown retrospectively and quantitative data derived from it.

I. Introduction

Synthetic aperture (SA) ultrasound imaging has for a number of years been developed for making high quality images due to its ability to employ dynamic focus in both transmit and receive for optimal point spread functions (PSF). Either spherical or plane waves are transmitted and the scattered signal is received on the elements of the probe [1–10]. The precise time of flight for the individual points can thereby be determined for all spatial positions ensuring optimal delay-and-sum focusing and coherent summation, resulting in dynamic focusing in both transmit and receive. The improved image quality has been demonstrated in a small clinical study [11]. Flow and motion imaging can also be performed using SA sequences [8, 10, 12, 13] giving major benefits in terms of continuous data everywhere in the region of interest. This has led to very high quality vector flow imaging [14], and the benefits have also been proved for plane wave transmissions [10] with improved sensitivity compared to normal sequential flow imaging [15, 16]. Sequences for low velocity flow have been developed [17] as well as sequences optimized for fast flow [18, 19]. It has also been demonstrated that non-linear imaging can be attained [20, 21]. Recently super resolution imaging has also been achieved with SA imaging [22–24].

These advantages for anatomic and flow SA imaging have been known for more than 20 years [8], but currently all of these applications employ different sequences, with different placements of the virtual source, different sequence lengths and timings. This paper will demonstrate that a single universal sequence can be used for all of the imaging schemes mentioned above, thus, yielding a complete data set in a single acquisition, where the acquired data retrospectively can be employed to yield all the different anatomic, functional, and super resolution images along with a range of quantitative parameters.

The demands on such a universal sequence are described in Section II, and the selection of virtual sources and their distribution is explained in Section III. The sequence has been implemented on a Verasonics research scanner for two linear array probes and on the experi-

mental scanner SARUS for a 384-elements linear array. Phantom and in vivo experiments on Sprague-Dawley rats have been conducted as described in Section IV as well as on a tissue mimicking flow phantoms with a 70% area constriction with pulsating flow and a carotid artery phantom. Examples from these measurements are shown in Section V, and the implications, limitations and further developments are elucidated in Section VI.

SA imaging can be attained with any wave that insonifies a major part of the region of interest. The most studied are spherical waves and plane waves, which are often called ultrafast imaging. The beamforming is slightly different for the transmit delay calculations, but the imaging is in principle the same. The paper will therefore restrict the treatment to spherical emissions, and similar optimizations can be employed for both wave types [25, 26].

II. REQUIREMENTS ON COMPLETE SA SEQUENCES

The various imaging modes mentioned in the introduction give rise to different criteria for their optimization. The demands are given below:

B-mode imaging: Here, the key parameters are resolution, primarily the Full-Width-Half-Max (FWHM) resolution R_{FWHM}, and contrast, which can be quantified as the ratio between main and side-lobe energy.

Here R_{FWHM} is estimated by

$$R_{FWHM} = \lambda F\# = \lambda \frac{D}{W} = \lambda \frac{D}{NP_e} = \lambda \frac{D}{N\lambda} = \frac{D}{N}, \quad (1)$$

where $F\# = \frac{D}{W}$ is the F-number, D is the imaging depth, W is the width of the aperture, N is the number of active elements, P_e is the pitch, which for a linear array often is the wavelength λ. The optimal resolution is, thus, determined by the number of elements in the aperture, demanding that the virtual source should be separated as much as possible in transmit, and that the full aperture should be employed in receive.

The contrast in the image is the ratio between the energy in the side-lobes relative to the total energy and is defined as:

$$CR(r) = 20\log_{10}\sqrt{\frac{E_{out}(r)}{E_{total}}}, \quad (2)$$

where E_{total} is the total energy in the point spread function and $E_{out}(r)$ is the energy beyond a radius of r [27]. This measure evaluates the contrast in the image, and $E_{out}(r)$ is calculated for a radius equal to 2.5λ.

This contrast is primarily determined by the number of transmissions, the number of receiving elements, the F-number and interpolation during beamforming. A high number of transmissions lowers the frame rate, and a

high number of receiving elements results in a high data bandwidth with large processing and storage demands in the scanner. A compromise must therefore be reached between these conflicting demands as investigated in Section III.

Flow imaging: Here two high resolution images (HRI) are correlated to yield the motion between the two [13]. The HRIs are created by beamforming a low resolution image (LRI) for the desired imaging region for each emission and then sum these LRIs for all the emissions. The maximum detectable velocity v_{max} is proportional to the wavelength divided by the effective time $T_{PRF,eff}$ between HRIs [18, 28]:

$$v_{max} \approx \lambda / T_{PRF,eff} \quad (3)$$

This necessitates a short time between images, and therefore sequences with few emissions are preferred. This will, however, reduce contrast and make it difficult to detect small vessels. A method for relaxing these requirements is to use interleaved [18] and permuted sequences, which can be employed in estimating the highest possible velocities as described in Section III-B.

Motion compensation: Coherently summing the LRIs acquired in SA imaging demands phase alignment. It has been demonstrated that motion compensation in 1-D [29] or 2-D [30] can increase image quality. This demands that tissue motion is estimated, but this is essentially the same processing as for flow imaging without echo canceling and is therefore optimized in the same way.

Low velocity imaging: The lowest velocity possible to estimate is essentially determined by the observation time usable in the echo canceling. The SA sequences should therefore be continuous, so data is available everywhere in the image at all times. The lowest velocity is then determined by the signal-to-noise ratio after echo canceling [31] and how still the probe can be held. This can often also be compensated for by tissue motion corrections as described above to extend the available time interval.

Non-linear imaging: Non-linear imaging uses the harmonics of the transmitted spectrum generated either by the non-linear ultrasound wave propagation or from a non-linear scattering contrast agent. The non-linear components can be isolated by either pulse inversion [32, 33] or amplitude modulation [34]. Both methods employ transmission of a number of consecutive pulses with a change in phase or amplitude to isolate the non-linear component by combining the received signals. This has also been demonstrated in SA imaging in [20, 21] and for contrast agent imaging in [35]. It will be shown that non-linear imaging can be combined with

interleaved flow imaging to yield sequences suitable for both imaging types.

Super resolution imaging: The universal sequence can also be used for super resolution imaging (SRI) with or without contrast agents [22, 23]. The emitted pressure has to be reduced to not disrupt the contrast agent, and the sequence must be used for both non-linear imaging of the agent and for finding the tissue motion for compensating the microbubble positions [36]. The sequence can also be used for SUper Resolution imaging using the Erythrocytes (SURE), where the full FDA range for the pressure emission can be used [24, 37].

Recursive imaging: The sequence should also support recursive imaging [38] , where a new high resolution image is generated after each emission. This can benefit motion estimation, where high resolution images from exactly the same emission sequence can be correlated, and the correlation functions averaged as detailed in [13] . This is also beneficial in super resolution imaging, where a number of high resolution image sequences equal to the number of emissions in the sequence can be recursively generated and all yield detections to decrease imaging time.

Functional imaging and derived metrics: The basic anatomic and functional motion images can also be used for deriving a number of useful metrics from the data. This includes pressure gradient estimation, tissue motion, elasticity, volume flow along with a larger range of other metrics [17, 39–42].

Deriving a universal sequence will, thus, make it possible to retrospectively select which images and metrics to show. It will allow switching between showing the anatomy and the functional images for more comprehensive diagnostics, and will supplement the current capabilities of ultrasound.

III. OPTIMIZING SEQUENCES

The optimization of SA sequences involves optimizing the placement of the virtual sources, the temporal order and repetition of the emissions, and the number of emitting elements and Sections detailing these optimizations are given below.

A. Spatial optimization

The first step in deriving a universal sequence is to ensure a near optimal B-mode image quality. SA imaging improves image quality by employing dynamic focusing in both transmit and receive [9]. It is performed by making a spherical transmission with a single or a collection of elements [5, 43]. The origin of the wave is therefore known precisely and can be used in the beamformation.
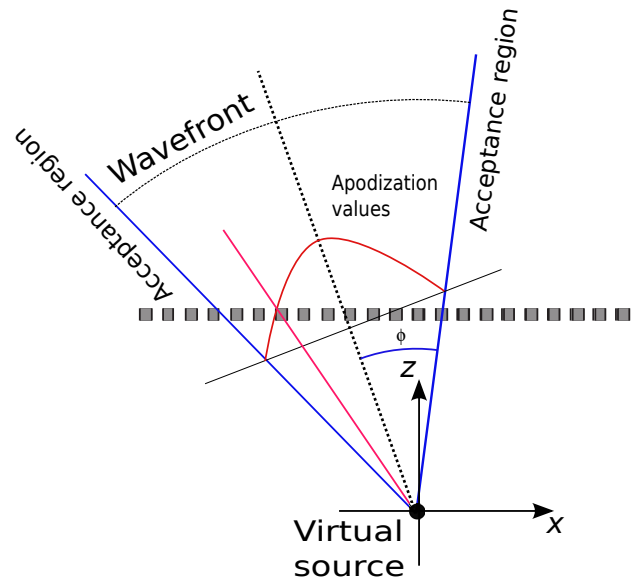

Fig. 1. Definition of a virtual source emitted in direction of the dashed line. The solid blue lines define the region for acceptable use of the emitted wave with the acceptance angle ϕ. The gray boxes are the elements, and the solid red line from the virtual source center through an element indicates from where the apodization value should be taken. Note that this virtual source has a negative F-number, as it is placed behind the aperture and emits a diverging wave.

The scattered signal is then received by all elements of the transducer. The path from transmission to reception can, thus, be precisely calculated. A full 2-D image of the object can be focused as the whole image region is insonified. This is a LRI, as it is only focused in receive. Repeating the process for all elements as transmitters and summing all the LRIs will yield a HRI, which has the best possible dynamical focus in both transmit and receive.

1) Design of virtual transmit sources: The proper design of the virtual transmit sources is vital for the SA image quality. In the beamforming it is assumed that the ultrasound emanates from the source, and that the field can be described as a spherical wave.

The virtual source is defined by the distance behind the aperture D, the width of the active aperture W, the steering angle θ, and the F-number, $F\# = D/W$, for the transmission. The F-number determines the acceptance angle given by [44]:

$$\phi = 2\arctan\left(\frac{1}{2|F\#|}\right). \qquad (4)$$

This indicates the angular span of the spherical wave emitted by the virtual source, where it can be predicted reliably. This is indicated at the acceptance region in Fig. 1. The span will often be smaller than the theoretical angle, due to the angular sensitivity of the individual

elements, especially for low F-numbers. The uniformity of the wave is also determined by the apodization of the active elements, which are determined by the F-number, $F\#$. For an un-steered virtual source the number of elements corresponds to $N_e = W/P_i$, where P_i is the element pitch.

An apodization is employed on each element to reduce edge effects and maintain a uniform spherical wave across the acceptance angle. Usually, a Hanning window is employed giving an apodization value a_i on element i as:

$$a_i = 0.5(1 - \cos(2\pi(1 + r_p)/2)) \qquad (5)$$

where r_p is the relative distance within the active aperture given by $r_p = (x_i - x_c)/W$. Here x_i is the element position, and x_c is the coordinate at the virtual elements center line, when it intersects the aperture (dashed line in Fig. 1). For $|r_p| > 1$ a_i is set to zero, as the element is outside the active aperture.

For a steered source the apodization values have to be projected onto the direction orthogonal to the steering direction. The angle between the line intersecting the element and the virtual source steering direction is:

$$\theta = \psi - \arctan\left(\frac{v_x - x_i}{v_z - z_i}\right), \qquad (6)$$

where (v_x, v_z) denotes the virtual source position, ψ is the steering angle, and (x_i, z_i) is the element position. The relative position is then given by:

$$r_p = \frac{D\arctan(\theta)}{D/(\cos(\theta)F\#)} = \arctan(\theta)\cos(\theta)F\#, \qquad (7)$$

which is inserted into the apodization calculation.

The delays imposed on the individual elements are determined by the distance from the virtual source to the element. They are calculated as:

$$\Delta t_i = \frac{|\vec{r}_i - \vec{r}_{vc}| - |\vec{r}_c - \vec{r}_{vc}|}{c}, \qquad (8)$$

where $\vec{r}_i$ is the element position, $\vec{r}_{vc}$ is the virtual source position, c is the speed of sound, and $\vec{r}_c$ is the point, where the center line of the virtual source is intersecting the aperture.

2) Optimized SA sequences: The contrast and resolution of a SA sequence are dependent on the number of virtual sources, their spread over the aperture, the interpolation method between samples during beamforming, and the transducer selected. This Section will show an example for a linear array and describes the various choices and their consequence for the sequence.

The basic principles for SA imaging and its optimization are described in [25, 26]. A linear array transducer with $\lambda/2$ pitch with 192 elements will be used as an
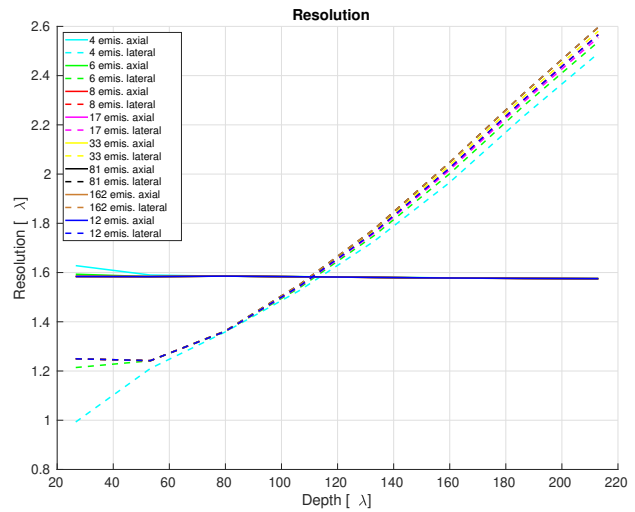

Fig. 2. Resolutions laterally and axially for different numbers of virtual source emissions. The selected sequence with 12 virtual sources is marked in blue.
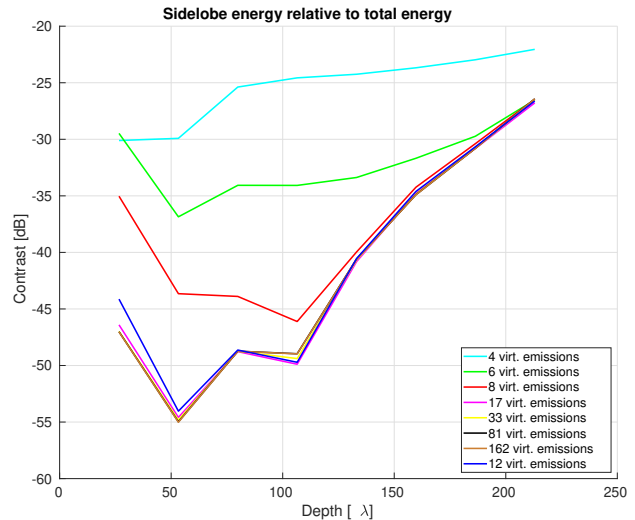

Fig. 3. Contrast ratios for different numbers of virtual source emissions for a phased array probe with $\lambda/2$ pitch and 192 elements. The selected sequence with 12 virtual sources is marked in blue.

example. Virtual sources behind the transducer (negative F-number) will be evenly distributed over the probe surface, and the optimization criteria are the Full-Width-Half-Max (FWHM) resolution axially and laterally along with the contrast ratio (CR) defined in (2).

The probe has a pitch of $\lambda/2$ to avoid grating lobes and have the maximum transmit acceptance angle. The virtual sources are un-steered to optimize the imaging in the rectangular region beneath the probe surface. Steering can be included to increase the field of view or increase signal-to-noise ratio by concentrating the transmitted energy in the imaging region beneath the array.
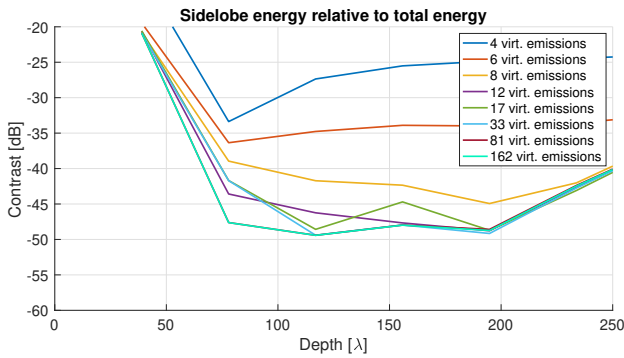
Fig. 4. Contrast ratios for different numbers of virtual source emissions for a linear array probe with λ pitch and 192 elements.

The focusing ability of the sequence is determined by three F-numbers: The transmit F-number for the virtual sources $F\#_v$, the F-number for synthesizing the transmit beam $F\#_t$, and finally the F-number for the receiving elements $F\#_r$. $F\#_v$ should also be as low possible to insonify the broadest possible region and still attain a coherent, spherical wavefront. This is determined by the element pitch, and an F-number of -0.5 can be attained for $\lambda/2$ pitch for a focus behind the array to create a diverging wave. For λ pitch, $F\#_v$ can be around -0.7. The F-numbers were determined by simulating the emitted field from the virtual source, and ensuring that the maximum delay deviation from the ideal spherical wavefront was less than $\pm 1/4 f_0$ to determine ϕ in (4) . Here f_0 is the center frequency of the probe. $F\#_t$ and $F\#_r$ are used in the dynamic beamforming for calculating the apodization profile for weighting of the virtual sources and weighting between the receiving elements. This is again determined by the element size and thereby their directivity, which give F-numbers of 0.5 for $\lambda/2$ pitch and 0.7 for λ pitch elements. All three F-numbers are set to 0.5 for $\lambda/2$ pitch probes and 0.7 for λ pitch probes throughout the paper.

The virtual sources are evenly distributed across the aperture to maintain the lowest possible F-number $F\#_t$ in transmit. Field II simulations [45, 46] for point targets have been conducted to reveal the influence of the number of virtual emission sources as shown in Fig. 2, where both the axial and lateral resolutions are shown. The number of sources has a negligible influence on the resolution, as they are optimally spread out over the aperture. The axial resolution is constant throughout depth and the lateral resolution increases with depth as the effective F-number increases proportional to depth.

The effect on the contrast is shown in Fig. 3 for a range of emissions for a phased array probe with $\lambda/2$ pitch and 192 elements. There is a large improvement in contrast

from emitting 4 to 12 times, especially for points close to the probe. Increasing from 12 to 162 virtual emissions gives a marginal improvement in image quality. A good compromise between frame rate and contrast is 12 to 33 virtual emissions, which will yield a frame rate 6 to 18 times higher than traditional imaging with an improved image quality, and which is only marginally worse than using 5 to 13 times as many emissions.

A similar plot is shown in Fig. 4 for a range of emissions for a linear array probe with λ pitch and 192 elements. A similar trend is seen with a large improvement in contrast when going from 4 to 12 emissions with negligible improvement for further increase in number of emissions. The near field point spread function has considerably higher side lobe levels due to the larger elements, but the contrast is kept over a larger depth, due to the larger array. The lowest side lobe levels are also higher than for the phased array, because of the larger elements, and the optimal array would be with $\lambda/2$ pitch and 384 elements.

B. Temporal optimization: Interleaved and permuted sequences

The second optimization of the SA sequence is to ensure an optimized temporal order and repetition of the emissions for motion detection.

Velocities and motions are found by correlating adjacent HRIs. The maximum detectable velocity v_{max} is inversely proportional to the time $T_{PRF,eff}$ between two HRIs, which should be minimized to attain the highest possible v_{max}. The minimum possible value is the time interval between pulse emissions T_{prf}, which can be attained by interleaving two HRIs by repeating the emissions as presented in [18, 19].

This approach also makes it possible to implement pulse inversion by inverting the second emission or amplitude modulation by manipulating the amplitude of the second emission. The correlation operation for flow estimation then just has to invert and amplify the second emission.

Interleaving, thus, breaks the relationship between the number of emissions in the SA sequence and v_{max}. The drawback is that the correlation time is doubled, and this can lead to de-correlation of the LRIs before summation. A possible solution is to employ motion correction before summation [29, 30] and in general keep the sequence length short.

Another possibility to diminish de-correlation is to reduce the time for making a HRI. This can be included in the sequence by permutation of the virtual source. A properly focused HRI should have the virtual sources

Position of virtual sources in transmit:
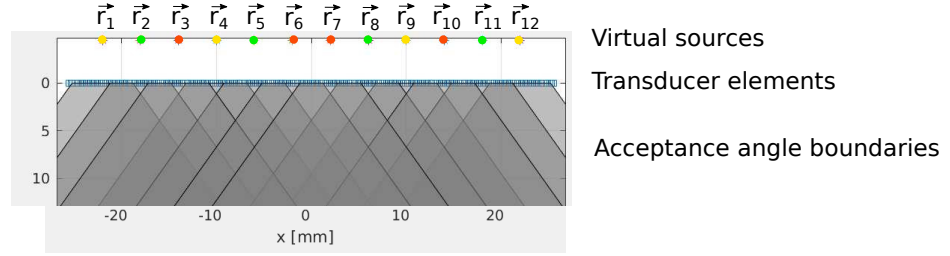
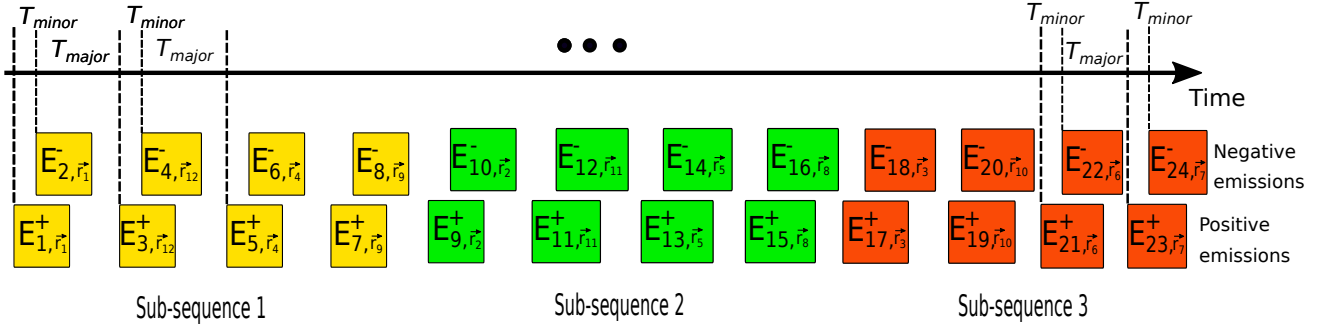**Timing of emission sequence:**

Fig. 5. Universal SA sequence for linear array probes using 12 virtual sources, interleaving with pulse inversion, and permutation. The top figure shows the linear, 192-elements array along with the placement of the virtual sources (colored circles) and their acceptance angles (gray lines). The lower image shows the timing of the sequence consisting of 2 times 12 emissions due to the pulse inversion with different colors for the three different sub-sequences. The lower row denotes the positive emissions and the upper row the negative emissions.

spread out over the aperture, and the 12 virtual sources could be ordered in three sub-sequences of four emissions, where each sub-sequence has the four emissions spread out over the aperture. This makes it possible to perform correlation after 2 times 4 emissions and would lower the de-correlation by a factor of 3. The correlation functions of the three groups could also be summed to increase precision. The drawback of this approach is a loss of contrast in each sub-sequence due to the averaging of fewer received emissions, and such an approach is best suited for large vessels with high velocities and correspondingly high de-correlation. Lower velocity flow for smaller vessels would benefit from employing all the emissions, and would not be impacted by the permutation.

C. Signal-to-noise optimization

The signal-to-noise ratio (SNR) in a SA sequence using de-focused emissions is proportional to [5, 47]:

$$\text{SNR} \propto M N_{T_s} N_{R_s} \tau_s \qquad (9)$$

where M is the number of transmissions, N_{T_s} is the number of transmit elements, N_{R_s} is the number of receiving elements, and τ_s is the temporal duration of the transmit signal. Increasing the number of transmit

elements will increase SNR, but will also decrease the effective transmit aperture by N_{T_s} elements, as the virtual source has to be placed further towards the center of the aperture. The FWHM in transmit will, thus, decrease, and that limits how many transmit elements should be used. The SNR is also directly proportional to the number of emissions, so longer sequences increase SNR, but this has to be balanced with the need for short sequences for motion estimation. Further τ_s can be increased, which lowers the axial resolution, if coded imaging is not used [48–50].

D. Universal sequence

The suggested universal sequence is shown in Fig. 5. The sequence contains 12 virtual sources evenly spread out over the full aperture as shown on the top image. The position of virtual source i is denoted by $\vec{r}_i$. Each virtual source is repeated with an inverted amplitude to enable pulse inversion and interleaved velocity estimation. An emission is denoted $E_{n,\vec{r}_i}^{+/-}$, where i denotes the virtual source number from 1 to 12, n is the emission number from 1 to 24, and the superscript sign denotes whether it is a positive or negative emission for pulse inversion. The virtual sources are permuted to have three short sub-sequences for high velocity flow, and the sequence
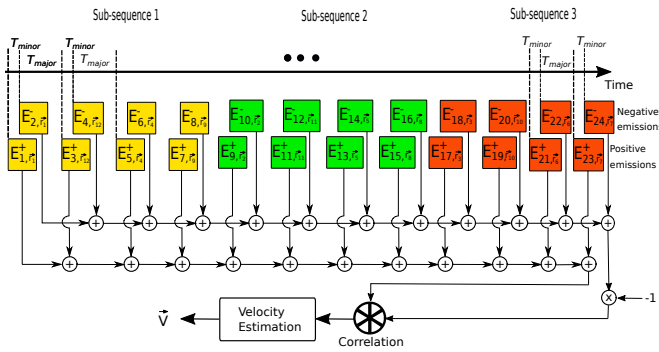
Fig. 6. Summation of the beamformed LRIs from the various emissions and sub-sequence correlation between the two HRIs in the complete sequence. The negative emissions are multiplied by -1 before the correlation to determine the velocity.

is continuously repeated for obtaining data suitable for low velocity flow and super resolution imaging [37]. The full sequence is shown in the lower image in Fig. 5, where yellow boxes denote the first sub-sequence, green the second, and red the third sub-sequence. The virtual sources are spread out over the aperture as much as possible for each sub-sequence, so for the first sub-sequence the virtual source positions start from the left most virtual source, then emit for the right most source, then a source in the middle left and finally in the middle right of the aperture. The same distribution is used for sub-sequence 2 and 3. The ordering of the virtual sources used is then: 1, 12, 4, 9, 2, 11, 5, 8, 3, 10, 6, 7.

The time interval between the emissions is often selected to be the same between all emissions and equal to T_{prf}. It can, however, be different for the various source to extend the time for the whole sequence and reduce the data rate. This is indicated in the lower time line in Fig. 5, where the time between positive and negative emissions, T_{minor}, is kept short for having the highest correlation and best suppression of the fundamental component in the pulse inversion, and a longer time, T_{major}, is used between different virtual sources. The sequence can also use other non-linear approaches like amplitude modulation. Here, three emissions are used for each virtual source [51–53], where all elements for the virtual source are used first, and then the odd and finally even elements emit.

The overall processing for finding motion or blood velocity is illustrated in Fig. 6 . The LRIs for the negative and positive emissions are each summed, and the HRI for the negative emissions is multiplied by -1 before being correlated with the HRI for the positive emissions to estimate the velocity. This can be performed for each line in the HRIs, but the correlation is often summed over a region of the image and over several HRIs to improve the

correlation estimate and, hence, the velocity or motion estimate. The value of T_{minor} in Fig. 5 determines the maximum detectable velocity, which is proportional to

$$v_{max} \propto \lambda / T_{minor}. \tag{10}$$

Having a low value of T_{minor}, thus, gives a high maximum detectable velocity and is only restricted by the imaging depth ($T_{minor} > 2D/c$, where D is the imaging depth).

In recursive imaging the last two emissions replace the two oldest ones, the correlation is calculated and averaged with previous correlation estimates to improve accuracy [13, 38]. Velocity estimation can also be made using only one of the sub-sequences for reducing motion artifacts during summing of the LRIs, with a reduction in contrast as a consequence.

Thirtytwo elements are used in de-focused transmissions for the virtual sources to have a good SNR and not limit the active transmit aperture too much.

The data rate and the amount of data can also be reduced by only sampling some of the elements during receive. This could be the sub-set of elements closest to the center of the virtual source. This will only affect the SNR, contrast and focusing for larger depths, where the acceptance angle is so large that elements outside the sampled ones should be included in the focusing.

IV. MEASUREMENT SETUP

The universal pulse inversion (PI) sequence with 2 x 12 virtual sources was implemented for both a 168-elements GE L8-18i, a 256-elements GE L3-12D, and a 192-elements GE 9L-D linear array probes (GE Medical, Chicago, IL, USA) connected to a Verasonics Vantage 256 scanner (Verasonics, Kirkland, WA, USA). All probes have a pitch of λ. The virtual sources were evenly distributed over the whole aperture and permuted in emission order for making flow estimation possible using 4, 8, or 12 virtual sources. The transmit frequency was 10 MHz for the GE L8-18i probe, and all 168 elements were sampled at sampling frequency f_s of 62.5 MHz with 14 bits precision. The frame rate was 208 Hz for fully independent images for a pulse repetition frequency f_{prf} of 5 kHz, and recursive imaging yielded 5,000 images per second. The GE L3-12D probe used a 6 MHz transmit frequency and the GE 9L-D used 7 MHz and for both f_s was 31.5 MHz. The GE L3-12D probe used a 2-1 multiplexing and the 128 elements closest to the center element of the transmitting virtual source were sampled during receive. An f_{prf} of 10 kHz was employed for a frame rate of 417 Hz.

Data were acquired on a 60% area reduction phantom with pulsating flow driven by a CompuFlow 1000
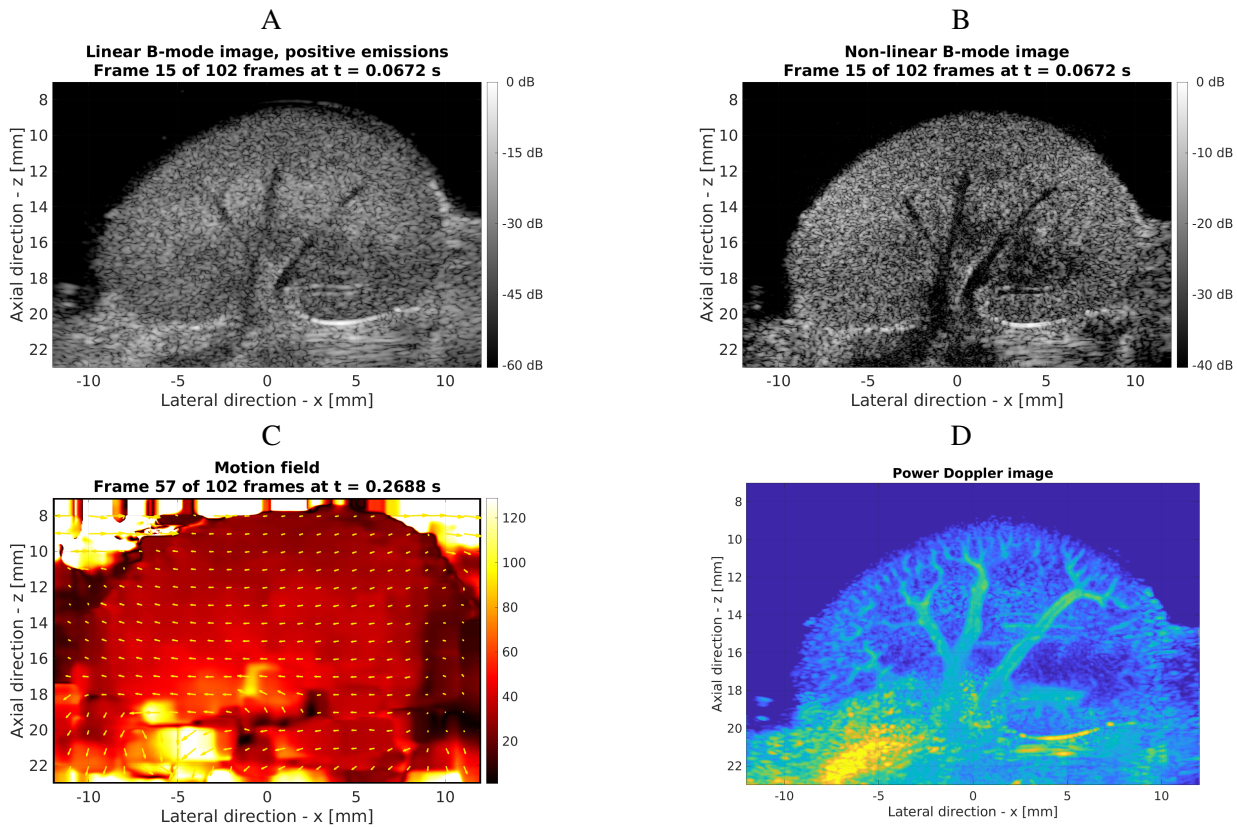
Fig. 7. Examples of in vivo images of a rat kidney using data acquired from a single interleaved, permuted pulse inversion sequence. The various images are: A - B-mode, B - non-linear, C - tissue motion, D - Power Doppler. The arrows in C indicate direction and magnitude of the motion. The brightness in D is proportional to the flow.

Flow System (Shelley Medical Imaging Technologies, Toronto, Ontario, Canada) using the cartoid2 pulse waveform. Data for 10 cardiac cycles of 840 ms were acquired, and the results from the cycles were aligned to reveal the relative standard deviation.

In vivo data from the kidney of an anesthetized Sprague-Dawley rat were acquired using the GE L8-18i probe directly on the exposed kidney. Data were acquired for 84 seconds and stored in RAM for later processing.

Data were also acquired using the SARUS experimental ultrasound scanner [54] with an experimental 384-elements $\lambda/2$ pitch linear array operating at 6 MHz. Here, a 3-D printed carotid bifurcation phantom was used [55–57] and the same 12×2 emissions sequence was employed with interleaving and permutation. The pulsating flow was identical to that used for the constriction phantom.

All data were beamformed using the GPU code developed in [58] for all imaging modes. The axial sampling interval was $\lambda/8$ and the lateral sampling interval was $\lambda/4$. Motion estimation for both tissue and blood velocity was made using the directional transverse oscillation (DTO) approach [59] using the auto-correlation

estimator [60]. The transverse oscillation was introduced by filtration in the frequency domain of the complex beamformed RF data as suggested in [61] with a lateral wavelength λ_x equal to 3λ and a lateral pulse length of 6λ.

V. IMAGING EXAMPLES

Four different examples of using the sequence are given in this Section. This includes in vivo examples from a rat kidney in Section V-A, phantom measurements on a constricted phantom with the GE linear array probe in Section V-B, carotid phantom examples for the 384-elements, $\lambda/2$ pitch linear array probe in Section V-C, and finally pressure difference estimation for the carotid phantom using the GE L3-12D probe.

A. In vivo example from a rat kidney

Imaging examples from the Sprague-Dawley rat kidney are shown in Fig. 7, where the top left (A) shows the anatomic B-mode image at a dynamic range of 60 dB. Employing both the positive and negative emissions yields the pulse inversion image shown on the top right (B).

The Field II simulated resolution for the linear setup at 22 mm is here 0.74λ in the lateral direction, the axial resolution is 0.59λ, and the contrast ratio is -56.7 dB using the positive emissions, which corresponds to the results obtained in Section III-A2. The 32-elements emissions gave a penetration of 410λ (SNR equal to 0 dB) for the linear array probe, when measured on a tissue mimicking phantom with an attenuation of 0.5 dB/[MHz cm].

The rat had a heart rate of 290 beats/min and was ventilated at 71 breaths/min. Averaging motion estimates over a 2 x 2 mm tissue region gives the motion data shown in Fig. 7C, where the arrows indicate motion components in the axial and lateral direction. Isolating the individual components gives a standard deviation of 1.06 μm and 2.06 μm for the axial and lateral motions for the heart beats and of 0.49 μm and 0.75 μm for the breathing motion [36].

These motion estimates can be used for tissue motion correction to fully align the tissue across all the images. The motion field as a function of space and time is used for correcting the RF signals for the LRIs back to the reference position using spline interpolation of the complex data, so they align as explained in[36, 37]. Then the tissue component can be removed by subtracting the images before and after the current image. Hereby, the flow is left and averaging across 2.3 seconds of data gives the power Doppler image shown in Fig. 7D.

The sequence can also be used for super resolution imaging using the erythrocytes (SURE) [24, 37]. Here, the tissue motion is estimated and used for aligning the LRIs before summation and echo canceling. Peaks in the flow image are then summed to reveal the SURE image as shown in Fig. 8, where the left image (A) uses the HRIs in detection. The right image (B) uses recursive imaging [38], where a new HRI is generated after each emission for a frame rate of 5000 Hz. This increases the number of detections by a factor of 24 for this sequence, and thereby increases the contrast in the image shown on the right.

B. Constricted phantom example

The 256-elements GE L3-12D linear array probe has been used for investigating the flow in a 3-D printed constriction phantom, and the corresponding images are shown in Fig. 9 for both color flow mapping (CFM) and DTO vector flow imaging. It can be seen how the CFM velocity estimates are very low, whereas the DTO estimates correctly depicts the blood velocity magnitude. The velocity estimates across several heart beats have been aligned as shown in Fig. 10 at the center of the constriction. The precision of the heart beats in terms of the mean standard deviation can be calculated from this and is 3.69 % (0.0161 m/s) compared to the peak velocity in the vessel of 0.49 m/s.

C. Phantom measurements using $\lambda/2$ pitch probe with sub-sequences

The PSF from using a larger $\lambda/2$ pitch probe with 384 elements is shown in Fig. 11. The data were acquired for all 384 elements using the SARUS scanner, and data were beamformed using an F-number of 0.5 for both transmission and reception giving a higher resolution than for the λ pitch probes. The lateral resolution was 0.57 λ and the side-lobe level was -44.9 dB, when measured on a wire phantom in water.

Vector flow in the carotid artery phantom at its bifurcation is shown in Fig. 12 on the top left when using the full sequence. One of the sub-sequences 1 to 3 in Fig. 5 can also be used for flow estimation. This is shown in the top right image for sub-sequence 3. Finding the SD over the 10 cardiac cycles for the measurement gives a relative SD for axial velocity of 5.3% (full) and 4.2% (sub) and 3.9% (full) and 5.1% (sub) for the lateral velocity, so the penalty of using the short sequence is marginal.

D. Functional imaging: Pressure difference estimation

The data acquired can also be used for functional imaging and for deriving various parameters from the flow data like peak and mean velocities, volume flows, resistive index and pressure difference. An example of this for the GE 9L-D linear array probe used on the carotid phantom is shown in Fig. 13 using the method described in [62]. Here, a starting point is selected in the image and a trajectory following the flow lines is automatically made. The pressure difference is then calculated between the end points, and the pressure difference as a function of time can be estimated as shown on the bottom figure for three cardiac cycles. The precision of the estimates is on the order of a few Pa. A starting point can be selected retrospectively in the data, and the uncertainty and invasiveness of placing a catheter is avoided.

VI. DISCUSSION AND IMPLICATIONS

It has been demonstrated that a single universal sequence can be devised for both anatomic, functional and super resolution imaging with near optimal performance for both the B-mode image and flow imaging. It can estimate the maximum detectable velocity as the time between HRIs is T_{prf} for a maximum velocity of $v_{max} \propto \lambda/T_{prf}$. This pulse repetition frequency is limited
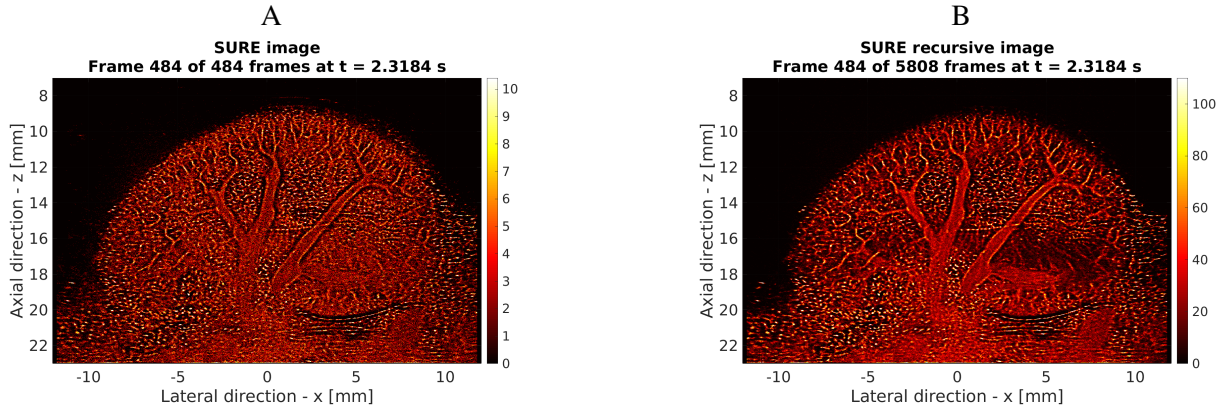
Fig. 8. Examples of in vivo super resolution images of a rat kidney using data acquired from the interleaved, permuted pulse inversion sequence. The left image shows the SURE image for the high resolution images and the right is when recursive imaging has been performed to increase the frame rate to 5000 Hz.
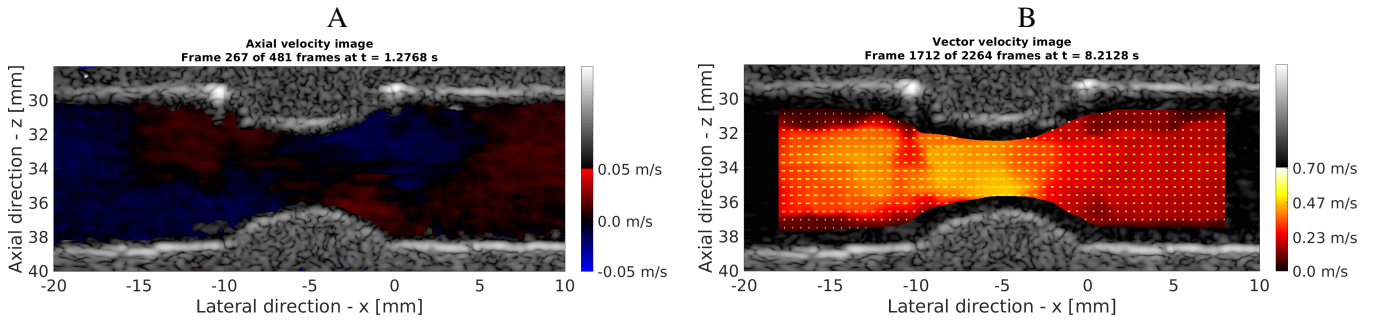

Fig. 9. Examples of color flow (A) and vector flow (B) images from the carotid artery phantom. The color values indicate velocity magnitude and the arrows in the right image indicates both direction and magnitude. The flow is near to perpendicular to the ultrasound propagation direction, and the axial components are therefore low.
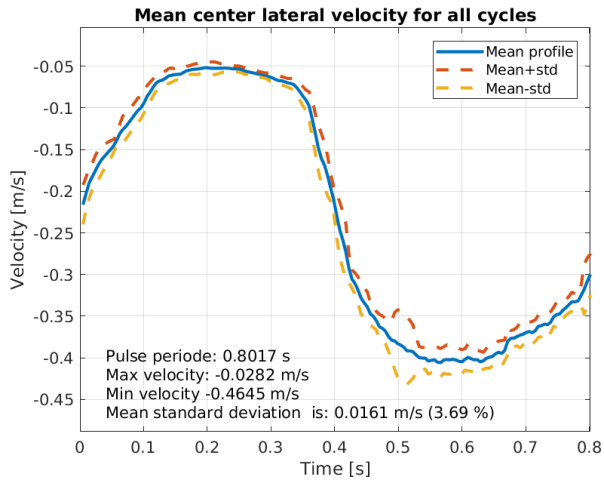

Fig. 10. Mean lateral velocity profile over time for 10 cardiac cycles at the center of the constriction in Fig. 9B.

Fig. 11. PSF from a wire phantom for the experimental 384-elements $\lambda/2$ pitch probe. The distance between the contour lines is 6 dB, and the resolution is 0.57 λ.

by the imaging depth D: $f_{prf} = 1/T_{prf} = c/(2D)$ and the maximum detectable velocity therefore equals that obtainable in conventional imaging, where data 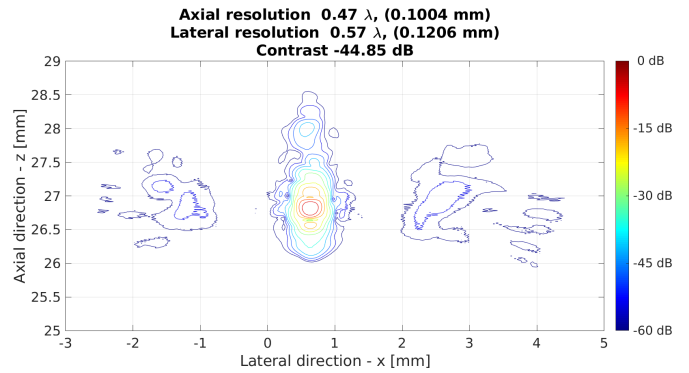only is acquired in one direction. The sequence is also continuous and has therefore no upper limit on the observation time for the data, which benefits both echo canceling and its ability to estimate low velocity flow and super resolution imaging.

This article has been accepted for publication in IEEE Transactions on Ultrasonics, Ferroelectrics, and Frequency Control. This is the author's version which has not been fully edited and content may change prior to final publication. Citation information: DOI 10.1109/TUFFC.2023.3280803
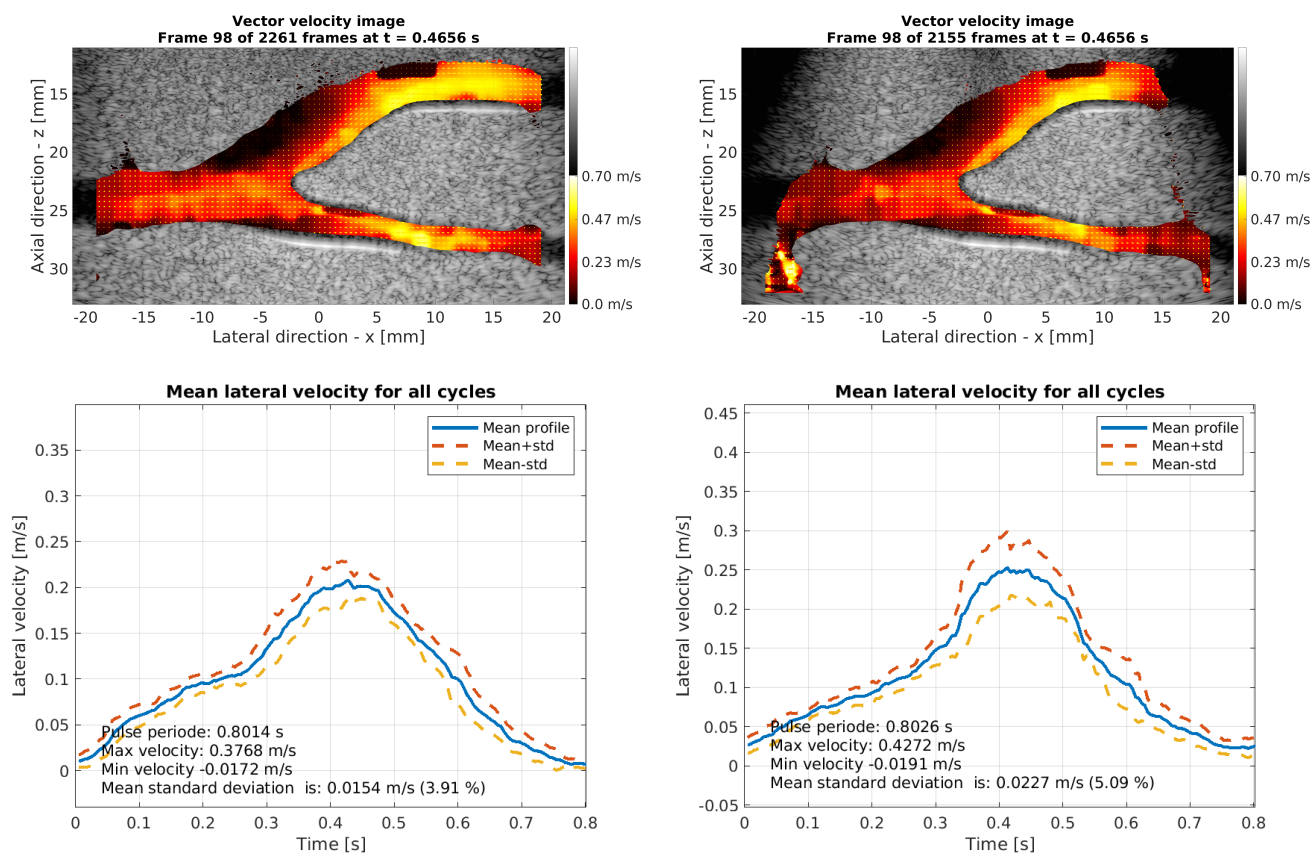
11

Fig. 12.   Vector flow images measured on a 3-D printed carotid artery phantom at its bifurcation. The top left shows the image when using all emissions in the sequence, and the top right is when using only the last sub-sequence with four emissions (the red emissions in Fig. 5). The two bottom plots show the corresponding performance for the lateral velocity component for the two sequences.

The imaging performed here employed spherical waves, but the same method can also be employed for plane waves. For a $\lambda/2$ pitch probe only 21 plane wave emissions were needed for optimal imaging in [25], and 32 emissions were needed for optimal SA imaging in [26]. Comprehensive simulation should be used to determine the optimal set of emissions taking number of plane waves and their angle span into account.

High velocities can also be estimated by just emitting from a single source as is used in ultra fast imaging, but the consequence is here that no transmit focusing is attained and the B-mode has a low quality and the contrast is low, hampering the detectability of small vessels. The developed sequence contains three sub-sequences with four emissions covering the full aperture. For shallow depths the image will have regions with gaps in the emitted fields for large arrays, few emissions sources, or large F-numbers in transmit for the sub-sequences, and this affects both anatomic and functional image quality. The problem can be mitigated based on the acceptance angle of the emitting sources as shown in the top image in Fig. 5 , by selecting the imaging depth

sufficiently large for the sources to cover the region of interest. This is demonstrated in Fig. 12 , where sub-sequence 3 yields roughly the same performance as the full sequence. Imaging closer to the probe will for the sub-sequences give artifacts as parts of the image is not insonified, and the full sequence has to be employed. This can be seen in the upper vessel branch on the right, where proper velocity estimates cannot be made, whereas deeper lying vessels placed at the image center have satisfactory estimates. The advantage of using the sub-sequence is the shorter averaging time, which reduces motion artifacts within the HRI. The drawback is the lower contrast as shown in Figs. 3 and 4 for few emissions.

Two arrays with λ and $\lambda/2$ pitch were simulated showing that the smaller pitch elements yielded lower side lobe levels especially close to the array. The side lobe levels are, however, maintained over a longer range of depths due to the larger λ pitch array, indicating that an optimal choice is the 384 elements $\lambda/2$ pitch array. This would entail more measurement channels, but this can potentially be leveraged by employing multiplexing
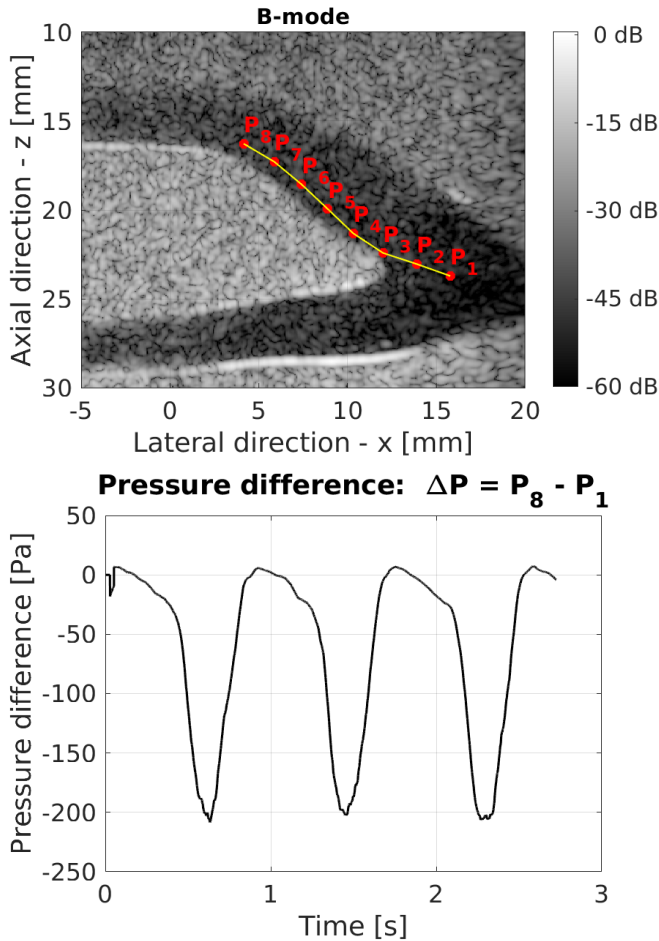
Fig. 13. Pressure difference estimation using the universal sequence. The top image shows the trajectory for the pressure gradient estimation, and the bottom image shows the estimated pressure difference between the two end points of the trajectory for three cardiac cycles.

as demonstrated in the 256-elements GE L3-12D linear array probe. Here, the 128 receiving elements closest to the virtual source were sampled.

The universal sequence suggested uses pulse inversion for non-linear imaging. It is also possible to use amplitude modulation for the non-linear part. This is often implemented for the binary transmitters used in the Verasonics scanner by having a full transmission with all elements and then having two emissions with the even and odd elements, respectively. This can also be used for universal imaging by combining the two last emissions into one and then assuming the time between emissions is $1.5 T_{prf}$. This will allow all imaging modes to be attained, although at a lower frame rate from the 3 emissions for a single virtual source.

The sequence devised here is not claimed to be optimal. It was shown that the 12 virtual sources yield a contrast close to the optimal SA contrast, when emit-

ting with all possible virtual sources, so only marginal optimization is probably possible.

The major benefit of such a sequence is the possibility of acquiring a complete data set usable for all common imaging modes with good precision, and that it can both be used for real time processing and also stored for later investigation. Retrospective processing can thereby yield any type of image and give precise quantitative metrics derivable from this.

REFERENCES

[1] J. J. Flaherty, K. R. Erikson, and V. M. Lund, "Synthetic aperture ultrasound imaging systems," United States Patent, US 3,548,642, 1967, united States Patent, US 3,548,642, 1967, Published 22 Dec 1970.

[2] C. B. Burckhardt, P.-A. Grandchamp, and H. Hoffmann, "An experimental 2 MHz synthetic aperture sonar system intended for medical use," *IEEE Trans. Son. Ultrason.*, vol. 21, no. 1, pp. 1–6, January 1974.

[3] M. O'Donnell and L. J. Thomas, "Efficient synthetic aperture imaging from a circular aperture with possible application to catheter-based imaging," *IEEE Trans. Ultrason. Ferroelec. Freq. Contr.*, vol. 39, pp. 366–380, 1992.

[4] J. T. Ylitalo and H. Ermert, "Ultrasound synthetic aperture imaging: Monostatic approach," *IEEE Trans. Ultrason. Ferroelec. Freq. Contr.*, vol. 41, pp. 333–339, 1994.

[5] M. Karaman, P. C. Li, and M. O'Donnell, "Synthetic aperture imaging for small scale systems," *IEEE Trans. Ultrason. Ferroelec. Freq. Contr.*, vol. 42, pp. 429–442, 1995.

[6] G. R. Lockwood, J. R. Talman, and S. S. Brunke, "Real-time 3-D ultrasound imaging using sparse synthetic aperture beamforming," *IEEE Trans. Ultrason. Ferroelec. Freq. Contr.*, vol. 45, pp. 980–988, 1998.

[7] R. Y. Chiao, L. J. Thomas, and S. D. Silverstein, "Sparse array imaging with spatially-encoded transmits," in *Proc. IEEE Ultrason. Symp.*, 1997, pp. 1679–1682.

[8] J. A. Jensen, S. I. Nikolov, T. Misaridis, and K. L. Gammelmark, "Equipment and methods for synthetic aperture anatomic and flow imaging," in *Proc. IEEE Ultrason. Symp.*, 2002, pp. 1555–1564.

[9] J. A. Jensen, S. Nikolov, K. L. Gammelmark, and M. H. Pedersen, "Synthetic aperture ultrasound imaging," *Ultrasonics*, vol. 44, pp. e5–e15, 2006.

[10] M. Tanter and M. Fink, "Ultrafast imaging in biomedical ultrasound," *IEEE Trans. Ultrason. Ferroelec. Freq. Contr.*, vol. 61, no. 1, pp. 102–119, January 2014.

[11] M. H. Pedersen, K. L. Gammelmark, and J. A. Jensen, "In-vivo evaluation of convex array synthetic aperture imaging," *Ultrasound Med. Biol.*, vol. 33, pp. 37–47, 2007.

[12] M. Tanter, J. Bercoff, L. Sandrin, and M. Fink, "Ultrafast compound imaging for 2-D motion vector estimation: application to transient elastography," *IEEE Trans. Ultrason. Ferroelec. Freq. Contr.*, vol. 49, pp. 1363–1374, 2002.

[13] S. I. Nikolov and J. A. Jensen, "In-vivo synthetic aperture flow imaging in medical ultrasound," *IEEE Trans. Ultrason. Ferroelec. Freq. Contr.*, vol. 50, no. 7, pp. 848–856, 2003.

[14] J. A. Jensen and S. I. Nikolov, "Directional synthetic aperture flow imaging," *IEEE Trans. Ultrason. Ferroelec. Freq. Contr.*, vol. 51, no. 9, pp. 1107–1118, 2004.

[15] J. A. Jensen, S. I. Nikolov, A. Yu, and D. Garcia, "Ultrasound vector flow imaging I: Sequential systems," *IEEE Trans. Ultrason. Ferroelec. Freq. Contr.*, vol. 63, no. 11, pp. 1704–1721, 2016.

[16] ——, "Ultrasound vector flow imaging II: Parallel systems," *IEEE Trans. Ultrason. Ferroelec. Freq. Contr.*, vol. 63, no. 11, pp. 1722–1732, 2016.

[17] E. Mace, G. Montaldo, B. Osmanski, I. Cohen, M. Fink, and M. Tanter, "Functional ultrasound imaging of the brain: Theory and basic principles," *IEEE Trans. Ultrason. Ferroelec. Freq. Contr.*, vol. 60, no. 3, pp. 492–506, 2013.

[18] J. A. Jensen, "Estimation of high velocities in synthetic aperture imaging: I: Theory," *IEEE Trans. Ultrason. Ferroelec. Freq. Contr.*, vol. 66, no. 6, pp. 1024–1031, 2019.

[19] ——, "Estimation of high velocities in synthetic aperture imaging: II: Experimental investigation," *IEEE Trans. Ultrason. Ferroelec. Freq. Contr.*, vol. 66, no. 6, pp. 1032–1038, 2019.

[20] M. Bae, H. Lee, S. B. Park, R. Yoon, M. H. Jeong, D. G. Kim, M. Jeong, and Y. Kim, "A new ultrasonic synthetic aperture tissue harmonic imaging system," in *Proc. IEEE Ultrason. Symp.*, 2008, pp. 1258–1261.

[21] M. C. Hemmsen, J. Rasmussen, and J. A. Jensen, "Tissue harmonic synthetic aperture ultrasound imaging," *J. Acoust. Soc. Am.*, vol. 136, no. 4, pp. 2050–2056, 2014.

[22] O. Couture, V. Hingot, B. Heiles, P. Muleki-Seya, and M. Tanter, "Ultrasound localization microscopy and super-resolution: A state of the art," *IEEE Trans. Ultrason. Ferroelec. Freq. Contr.*, vol. 65, no. 8, pp. 1304–1320, 2018.

[23] K. Christensen-Jeffries, O. Couture, P. A. Dayton, Y. C. Eldar, K. Hynynen, F. Kiessling, M. O'Reilly, G. F. Pinton, G. Schmitz, M. Tang *et al.*, "Super-resolution ultrasound imaging," *Ultrasound Med. Biol.*, vol. 46, no. 4, pp. 865–891, 2020.

[24] J. A. Jensen, M. Schou, S. B. Andersen, S. B. Søgaard, C. M. Sørensen, M. B. Nielsen, C. Gundlach, H. M. Kjer, A. B. Dahl, M. B. Stuart, and B. G. Tomov, "Fast super resolution ultrasound imaging using the erythrocytes," in *Proc. SPIE Med. Imag.*, vol. 12038, 2022, p. 120380E.

[25] J. Jensen, M. B. Stuart, and J. A. Jensen, "Optimized plane wave imaging for fast and high-quality ultrasound imaging," *IEEE Trans. Ultrason. Ferroelec. Freq. Contr.*, vol. 63, no. 11, pp. 1922–1934, 2016.

[26] R. Moshavegh, J. Jensen, C. A. Villagomez-Hoyos, M. B. Stuart, M. C. Hemmsen, and J. A. Jensen, "Optimization of synthetic aperture image quality," in *Proc. SPIE Med. Imag.*, vol. 9790, 2016, pp. 97 900Z–97 900Z–9.

[27] K. Ranganathan and W. F. Walker, "Cystic resolution: A performance metric for ultrasound imaging systems," *IEEE Trans. Ultrason. Ferroelec. Freq. Contr.*, vol. 54, no. 4, pp. 782–792, 2007.

[28] J. A. Jensen, *Estimation of Blood Velocities Using Ultrasound: A Signal Processing Approach*. New York: Cambridge University Press, 1996.

[29] L. F. Nock and G. E. Trahey, "Synthetic receive aperture imaging with phase correction for motion and for tissue inhomogenities - part I: basic principles," *IEEE Trans. Ultrason. Ferroelec. Freq. Contr.*, vol. 39, pp. 489–495, 1992.

[30] K. L. Gammelmark and J. A. Jensen, "2-D tissue motion compensation of synthetic transmit aperture images," *IEEE Trans. Ultrason. Ferroelec. Freq. Contr.*, vol. 61, no. 4, pp. 594–610, April 2014.

[31] C. Demene, T. Deffieux, M. Pernot, B.-F. Osmanski, V. Biran, J.-L. Gennisson, L.-A. Sieu, A. Bergel, S. Franqui, J.-M. Correas, I. Cohen, O. Baud, and M. Tanter, "Spatiotemporal clutter filtering of ultrafast ultrasound data highly increases Doppler and fUltrasound sensitivity," *IEEE Trans. Med. Imag.*, vol. 34, no. 11, pp. 2271–2285, 2015.

[32] P. N. Burns, D. H. Simpson, and M. A. Averkiou, "Nonlinear imaging," *Ultrasound Med. Biol.*, vol. 26, no. Suppl. 1, pp. 19–22, May 2000.

[33] D. H. Simpson, C. T. Chin, and P. N. Burns, "Pulse inversion Doppler: A new method for detecting nonlinear echoes from microbubble contrast agents," *IEEE Trans. Ultrason. Ferroelec. Freq. Contr.*, vol. 46, no. 2, pp. 372–382, 1999.

[34] G. A. Brock-Fischer, M. D. Poland, and P. G. Rafter, "Means for increasing sensitivity in non linear ultrasound systems," US Patent (5577505), 1996.

[35] O. Couture, S. Bannouf, G. Montaldo, J. Aubry, M. Fink, and M. Tanter, "Ultrafast imaging of ultrasound contrast agents," *Ultrasound Med. Biol.*, vol. 35, no. 11, pp. 1908–1916, 2009.

[36] I. Taghavi, S. B. Andersen, C. A. V. Hoyos, M. B. Nielsen, C. M. Sørensen, and J. A. Jensen, "In vivo motion correction in super resolution imaging of rat kidneys," *IEEE Trans. Ultrason. Ferroelec. Freq. Contr.*, vol. 68, no. 10, pp. 3082–3093, 2021.

[37] J. A. Jensen, M. Schou, S. B. Andersen, B. G. Tomov, S. B. Søgaard, C. M. Sørensen, M. B. Nielsen, C. Gundlach, H. M. Kjer, A. B. Dahl, and M. B. Stuart, "In vivo super resolution ultrasound imaging using the erythrocytes - SURE," *Proc. IEEE Ultrason. Symp.*, pp. 1–4, 2022.

[38] S. I. Nikolov, K. Gammelmark, and J. A. Jensen, "Recursive ultrasound imaging," in *Proc. IEEE Ultrason. Symp.*, vol. 2, 1999, pp. 1621–1625.

[39] J. B. Olesen, M. S. Traberg, M. J. Pihl, and J. A. Jensen, "Noninvasive estimation of 2-D pressure gradients in steady flow using ultrasound," *IEEE Trans. Ultrason. Ferroelec. Freq. Contr.*, vol. 61, no. 8, pp. 1409–1418, 2014.

[40] J. Jensen, J. B. Olesen, M. B. Stuart, P. M. Hansen, M. B. Nielsen, and J. A. Jensen, "Vector velocity volume flow estimation: Sources of error and corrections applied for arteriovenous fistulas," *Ultrasonics*, vol. 70, pp. 136–146, 2016.

[41] J. Ophir, I. Céspedes, H. Ponnekanti, Y. Yazdi, and X. Li, "Elastography: A quantitative method for imaging the elasticity of biological tissues," *Ultrason. Imaging*, vol. 13, no. 2, pp. 111–134, 1991.

[42] J. Bercoff, M. Tanter, and M. Fink, "Supersonic shear imaging: A new technique for soft tissue elasticity mapping," *IEEE Trans. Ultrason. Ferroelec. Freq. Contr.*, vol. 51, no. 4, pp. 396–409, 2004.

[43] C. H. Frazier and W. D. O'Brien, "Synthetic aperture techniques with a virtual source element," *IEEE Trans. Ultrason. Ferroelec. Freq. Contr.*, vol. 45, no. 1, pp. 196–207, 1998.

[44] N. Oddershede and J. A. Jensen, "Effects influencing focusing in synthetic aperture vector flow imaging," *IEEE Trans. Ultrason. Ferroelec. Freq. Contr.*, vol. 54, no. 9, pp. 1811–1825, 2007.

[45] J. A. Jensen and N. B. Svendsen, "Calculation of pressure fields from arbitrarily shaped, apodized, and excited ultrasound transducers," *IEEE Trans. Ultrason. Ferroelec. Freq. Contr.*, vol. 39, no. 2, pp. 262–267, 1992.

[46] J. A. Jensen, "Field: A program for simulating ultrasound systems," *Med. Biol. Eng. Comp.*, vol. 10th Nordic-Baltic Conference on Biomedical Imaging, Vol. 4, Supplement 1, Part 1, pp. 351–353, 1996.

[47] K. L. Gammelmark and J. A. Jensen, "Multielement synthetic transmit aperture imaging using temporal encoding," *IEEE Trans. Med. Imag.*, vol. 22, no. 4, pp. 552–563, 2003.

[48] T. Misaridis and J. A. Jensen, "Use of modulated excitation

This article has been accepted for publication in IEEE Transactions on Ultrasonics, Ferroelectrics, and Frequency Control. This is the author's version which has not been fully edited and content may change prior to final publication. Citation information: DOI 10.1109/TUFFC.2023.3280803

14

signals in ultrasound, Part I: Basic concepts and expected benefits," *IEEE Trans. Ultrason. Ferroelec. Freq. Contr.*, vol. 52, pp. 192–207, 2005.

[49] ——, "Use of modulated excitation signals in ultrasound, Part II: Design and performance for medical imaging applications," *IEEE Trans. Ultrason. Ferroelec. Freq. Contr.*, vol. 52, pp. 208–219, 2005.

[50] ——, "Use of modulated excitation signals in ultrasound, Part III: High frame rate imaging," *IEEE Trans. Ultrason. Ferroelec. Freq. Contr.*, vol. 52, pp. 220–230, 2005.

[51] R. J. Eckersley, C. T. Chin, and P. N. Burns, "Optimising phase and amplitude modulation schemes for imaging microbubble contrast agents at low acoustic power," *Ultrasound Med. Biol.*, vol. 31, no. 2, pp. 213–219, 2005.

[52] D. Fouan and A. Bouakaz, "Investigation of classical pulse sequences for contrast-enhanced ultrasound imaging with a CMUT probe," *IEEE Trans. Ultrason. Ferroelec. Freq. Contr.*, vol. 63, no. 10, pp. 1496–1503, 2016.

[53] S. H. Øygard, M. L. Ommen, B. G. Tomov, S. E. Diederichsen, E. V. Thomsen, M. B. Stuart, N. B. Larsen, and J. A. Jensen, "Contrast-enhanced ultrasound imaging using capacitive micromachined ultrasonic transducers," *J. Acoust. Soc. Am.*, vol. 153, no. 3, pp. 1887–1897, 2023.

[54] J. A. Jensen, H. Holten-Lund, R. T. Nilsson, M. Hansen, U. D. Larsen, R. P. Domsten, B. G. Tomov, M. B. Stuart, S. I. Nikolov, M. J. Pihl, Y. Du, J. H. Rasmussen, and M. F. Rasmussen, "SARUS: A synthetic aperture real-time ultrasound system," *IEEE Trans. Ultrason. Ferroelec. Freq. Contr.*, vol. 60, no. 9, pp. 1838–1852, 2013.

[55] S. S. M. Lai, B. Y. S. Yiu, A. K. K. Poon, and A. C. H. Yu, "Design of anthropomorphic flow phantoms based on rapid prototyping of compliant vessel geometries," *Ultrasound Med. Biol.*, vol. 39, no. 9, pp. 1654–1664, 2013.

[56] J. B. Olesen, C. A. Villagómez Hoyos, N. D. Møller, C. Ewertsen, K. L. Hansen, M. B. Nielsen, B. Bech, L. Lönn, M. S. Traberg, and J. A. Jensen, "Non-invasive estimation of pressure changes using 2-D vector velocity ultrasound: An experimental study with in-vivo examples," *IEEE Trans. Ultrason. Ferroelec. Freq. Contr.*, vol. 65, no. 5, pp. 709–719, 2018.

[57] S. Holbek, K. H. Lindskov, H. Bouzari, C. Ewertsen, M. B. Stuart, C. Thomsen, M. B. Nielsen, and J. A. Jensen, "Common carotid artery flow measured by 3-D ultrasonic vector flow imaging and validated with magnetic resonance imaging," *Ultrasound Med. Biol.*, vol. 43, no. 10, pp. 2213–2220, 2017.

[58] M. B. Stuart, P. M. Jensen, J. T. R. Olsen, A. B. Kristensen, M. Schou, B. Dammann, H. H. B. Sørensen, and J. A. Jensen, "Real-time volumetric synthetic aperture software beamforming of row-column probe data," *IEEE Trans. Ultrason. Ferroelec. Freq. Contr.*, vol. 68, no. 8, pp. 2608–2618, 2021.

[59] J. A. Jensen and P. Munk, "A new method for estimation of velocity vectors," *IEEE Trans. Ultrason. Ferroelec. Freq. Contr.*, vol. 45, no. 3, pp. 837–851, 1998.

[60] J. A. Jensen, "A new estimator for vector velocity estimation," *IEEE Trans. Ultrason. Ferroelec. Freq. Contr.*, vol. 48, no. 4, pp. 886–894, 2001.

[61] M. Lenge, A. Ramalli, E. Boni, H. Liebgott, C. Cachard, and P. Tortoli, "High-frame-rate 2D vector blood flow imaging in the frequency domain," *IEEE Trans. Ultrason. Ferroelec. Freq. Contr.*, vol. 61, no. 9, pp. 1504–1514, 2014.

[62] L. E. Haslund, L. T. Jørgensen, M. S. Traberg, M. B. Stuart, and J. A. Jensen, "Precise estimation of intravascular pressure gradients," *IEEE Trans. Ultrason. Ferroelec. Freq. Contr.*, vol. 70, no. 5, pp. 393–405, May 2023.

Jørgen Arendt Jensen (M'93-SM'02-F'12) received the MSc degree in 1985, the Ph.D. degree in 1989, and the Dr.Techn. degree all from the university in 1996. Since 1993, he has been a Full Professor of Biomedical Signal Processing with the Department of Electrical Engineering, Technical University of Denmark. He has been the founder and head of the Center for Fast Ultrasound Imaging since its inauguration in 1998. CFU has contributed with innovations in transverse oscillation vector flow imaging, synthetic aperture flow imaging in 2D and 3D, ultrasound simulation, research scanners, and row-column probes and beamforming. He has published more than 500 journal and conference papers on signal processing and medical ultrasound and the book Estimation of Blood Velocities Using Ultrasound (Cambridge Univ. Press), 1996. He is also the developer and maintainer of the Field II simulation program. He has been a visiting scientist at Duke University, Stanford University, and the University of Illinois at Urbana-Champaign. He was founder and head of the Biomedical Engineering group from 2007 to 2010. In 2003, he was one of the founders of the biomedical engineering program in Medicine and Technology, which is a joint degree program between the Technical University of Denmark and the Faculty of Health and Medical Sciences at the University of Copenhagen. The degree is one of the most sought-after engineering degrees in Denmark. He was chairman of the study board from 2003 to 2010 and Adjunct Professor with the University of Copenhagen from 2005 to 2010. He has given a number of short courses on simulation, synthetic aperture imaging, and flow estimation at international scientific conferences and teaches biomedical signal processing and medical imaging at the Technical University of Denmark. His research is centered around simulation of ultrasound imaging, synthetic aperture imaging, super resolution imaging, vector blood flow estimation, 3D imaging, row-column probes, and construction of ultrasound research systems. Dr. Jensen has given more than 60 invited talks at international meetings and received several awards for his research, most recently the Grand Solutions Prize from the Danish Minister of Science, the order of the Dannebrog by her Majesty the Queen of Denmark, and the 2019 Rayleigh award by the IEEE UFFC society.

Borislav G. Tomov received the M.Sc. degree in electronics engineering from the Technical University of Sofia, Sofia, Bulgaria, in 1996, and the Ph.D. degree in medical electronics from the Technical University of Denmark, Kongens Lyngby, Denmark, in 2003. He is currently a Senior Researcher with Center for Fast Ultrasound Imaging, Department of Health Technology, Technical University of Denmark. His research interests include medical ultrasound signal processing and ultrasound scanner architectures and implementations.

n spLars Emil Haslund (Graduate Student Member, IEEE) received the M.Sc. degree in biomedical engineering from the Technical University of Denmark (DTU), Lyngby, Denmark, in 2020, where he is currently pursuing the Ph.D. degree with the Center for Fast Ultrasound Imaging, Department of Health Technologies. His research topics include non-invasive pressure gradient estimations using synthetic aperture ultrasound.

Nathalie Sarup Panduro earned her master's degree in medicine from the University of Copenhagen in 2015. Currently pursuing a Ph.D. in clinical and preclinical super-resolution ultrasound imaging, Nathalie collaborates with the Department of Biomedical Sciences at the University of Copenhagen and the Center for Fast Ultrasound Imaging at the Technical University of Denmark. Her research focuses on developing advanced diagnostic imaging tools for clinical applications.

Charlotte Mehlin Sørensen received her B.Sc. in Biology from University of Copenhagen, Denmark in 1996. In 1999, she received her M.Sc. in Human Biology. She completed her PhD in Renal Physiology in 2004 and continued as Assistant Professor at UCPH until 2006 where she joined the medical company Zealand Pharma as a drug discovery scientist focusing on acute kidney injury. She returned to UCPH in 2007 and became Associate Professor in Renal Physiology in 2011. Her research focuses on renal hemodynamics and the interplay between the renal autoregulatory mechanisms and the topology of the renal vascular tree and includes the regulatory roles of gap junctions, potassium channels and incretin hormones.